Contents lists available at ScienceDirect

Nano Energy

Stencil-printed Lithium-ion micro batteries for IoT applications

Anju Toor [a],[*], Albert Wen [b], Filip Maksimovic [a], Abhinav M. Gaikwad [a], Kristofer S.J. Pister [a], Ana C. Arias [a]

[a] Department of Electrical Engineering and Computer Sciences, University of California Berkeley, Berkeley, CA, United States
[b] Department of Mechanical Engineering, University of California Berkeley, Berkeley, CA, United States

ARTICLE INFO

ABSTRACT

A battery design and fabrication process is demonstrated to make Lithium-ion (Li-ion) microbatteries with high capacity to power IoT devices. The battery consists of printed anode and cathode layers based on graphite and lithium cobalt oxide (LCO) respectively. The active area of the electrodes is scaled down to 1 mm^2 and the resulting electrochemical performance is evaluated. These miniature batteries demonstrate a significantly higher discharge capacity (6.4 mAh/cm^2) and energy density (23.6 mWh/cm^2) than thin-film and thick-film, and 3D microbatteries. This work shows a miniaturized Li-ion battery capable of powering a MEMS-based wireless sensor system with peak current requirements as high as 4 mA, demonstrating its effectiveness as a power source for integrated electronics.

1. Introduction

The rapid growth of the electronics industry has resulted in a sustained need for portable electronics. Significant effort has been directed towards developing miniaturized devices for applications in wireless sensor networks [1], biomedical sensors [2], gas sensors [3], actuators [4,5] and wearables [6,7]. In particular, due to a rise in the popularity of the Internet of Things (IoT), demand for "autonomous wireless sensors" has increased. These devices can be used for smart building control, industrial process automation, factory automation, and many other applications. Such devices require integrated i.e., on-board power sources to be able to provide stable current supply and to deliver high peak currents on the order of ~1–10 mA while occupying small areas (< 1 cm^2). Recent work has shown that with the exception of the power supply, all of the components needed for standards-compatible wireless communication can be integrated onto a single silicon chip with a wirebond antenna [8]. Printing the power supply directly on such a chip at wafer-scale would be a low-cost, small-volume solution. Rechargeable batteries (e.g., a Li-ion battery system) are preferred candidates due to their high energy density and long cycle life [9–12]. The commercially available low footprint batteries use semiconductor processing tools (therefore, costly) and lack enough capacity to power IoT devices. Despite the popularity and widespread demand for miniature wireless devices, limited advances have been made to design energy storage mechanisms that can satisfy their power and size requirements[13].

For miniature or scaled-down Li-ion batteries, three key battery configurations have been adopted, thin-film [14–18], thick-film [19–23], and 3D architectures [24–34]. Typically, thin-film Li-ion batteries are configured from successive thin film depositions using processes such as sputtering [35–38], chemical vapor deposition [39], and pulsed laser deposition [40]. Previously, thin-film planar battery configurations with either the cathode and anode layers stacked on top of one another (layer by layer) or deposited side by side on the respective current collectors have been demonstrated [41–44]. A vertical architecture i.e., layer by layer configuration, allows reducing the battery footprint area, which is critical for wireless miniaturized electronic device applications. Although most of these processes are compatible with microelectronic device fabrication, the thicknesses of the active layers prepared by these thin-film techniques are limited to 1–5 μm due to issues such as fracture, adhesion, high internal resistance [21], and slow diffusion of Li^+ ions in solid films. This results in insufficient power and capacity per unit footprint area to allow the operation of microelectronic devices.

Thick-film battery configurations employ printing processes such as stencil printing [20,45], laser-direct write technique (LDW) [21,22,26], etc. to allow the fabrication of porous structured thick-film electrodes without requiring any lithographic patterning. Owing to their porous structure, these electrodes could provide significantly higher areal capacities than the thin-film electrodes. This in turn allows for improved ionic and electron transport through the thick electrodes.

---

* Corresponding author.

E-mail address: atoor@berkeley.edu (A. Toor).

3D battery architectures involve 3D electrodes in several forms such as arrays of microrods/microtubes synthesized by the templating method [46,47], micro/nanowires [48,49], interdigitated [29,50], honeycomb-like and sponge-like [51]. 3D structural designs tend to overcome the limitations of thin-film battery configurations by offering high energy density without increasing the Li-ion diffusion lengths for a given footprint area. However, the fabrication of 3D battery architectures is often quite complex and restricted to very few cathode and anode materials. For example, consider the templating method [47], which involves microfabrication of a base array to act as the mechanical support and sequential deposition of a series of layers representing electrolyte, active material, and current collectors, etc. The outstanding challenge here is the development of deposition techniques that result in conformal and pin-hole free films for the different layers that comprise the battery stack [47]. Further, their fabrication cost and time is significant when compared to traditional batteries.

One promising approach to develop high capacity miniature/micro Li-ion batteries is to employ printing methods such as stencil and screen printing to deposit thick, high capacity electrodes [20]. In this paper, the batteries with active area < 25 mm^2 are referred to as micro-batteries. In conventional battery fabrication processes, the electrode slurry is deposited with blanket coating methods. However, with the stencil/screen printing method, the slurry can be deposited over a well-defined area. Typically, electrode films with a thickness on the order of 100 μm can be obtained. Batteries manufactured using print technologies offer the advantage that they can be directly printed on the electronic device during the device fabrication. Printing methods [20, 52–54] also provide the flexibility to customize battery active area as per the device layout and size requirements while also accommodating a wide range of substrate materials, ranging from flexible plastics to rigid substrates e.g., silicon. Therefore, printed batteries incorporating additive manufacturing methods to achieve low-cost fabrication [55–57] and high throughput are excellent candidates for supporting the power requirements of wireless electronic systems. Although a significant amount of work has been performed on printed batteries for large-area applications [54–60], reports focused on scaling battery size and power for typical IoT system requirements are limited [20,29,30,61].

In this work, a battery design and fabrication process is demonstrated to address the lack of low footprint, high-capacity microbatteries for MEMS-based sensors. The battery consists of synthetic graphite and lithium cobalt oxide (LCO) as the respective anode and cathode layers printed on thin evaporated current collectors. For the fabrication of batteries, a vertical configuration is adopted where single layers of anode, separator, and cathode are stacked and sealed together. Once printed, the batteries are assembled and packaged using an airtight seal (Torr Seal®) in a glovebox and tested in air. This work investigates the electrochemical limitations of Li-ion batteries as the active areas are scaled-down. The areal capacity as a function of the electrode area (1–25 mm^2) is evaluated, and the influence of the electrode film thickness on the battery performance is studied. The batteries demonstrate an areal capacity as high as ~6.4 mAh/cm^2, capacity retention >80% and columbic efficiency >97% under 30 charge/discharge cycles. Our experiments show that a 25 mm^2 battery can power a wireless transceiver chip, single-chip micro mote (SCμM) [8] that consumes a baseline current of 650 μA with a peak current as high as ~ 4 mA.

2. Results and discussion

2.1. Battery architecture and processing

2.1.1. Electrode materials and preparation

Lithium cobalt oxide (LCO) and synthetic graphite electrochemistry is selected for the printed, miniature Li-ion battery due to its stable electrochemical performance. The battery system comprises of LCO cathode and graphite anode with an organic electrolyte 1 M LiPF$_6$ in EC/DEC (1:1). Aluminum (Al) and copper (Cu) were used as the current collectors for the cathode and anode, respectively. Current collector layers serve the dual purpose of providing mechanical support to the active materials and facilitating efficient charge transfer to and from the battery. The theoretical specific capacities of the LCO and graphite are 145 and 350 mAh/g, respectively. The batteries were designed to be cathode limited to prevent the deposition of lithium metal during the charging step. Hence, the expected battery capacity and utilization were defined by the weight of the LCO film.

The stencil printing process is developed to achieve thick electrode films with areas as small as 1 mm^2. In the stencil printing process, a stencil with the desired pattern is placed in contact with the substrate, followed by dispensing of ink, which is then pushed into the stencil with the help of a doctor blade. Once the blade is traversed over the stencil opening, the stencil is removed, and the pattern from the stencil is transferred onto the substrate. Fig. 1 (A) shows a schematic illustration of the stencil printing process; here, cathode slurry is deposited through a polyimide plastic stencil on the glass substrate. In this work, cathode, and anode active layers are stencil printed on top of the respective current collector layers.

2.1.2. Electrode composition and optimization

To obtain high capacity batteries with a device compatible areal footprint, electrode ink must be carefully designed to meet the performance and processing criteria. The electrode inks with high active mass loadings will provide higher capacity, and typically consist of active particles, conductive additives, and a polymer binder. Typically, the solid content is fixed to reflect the final composition and the solvent content/binder molecular weight is adjusted to get the desired rheology. The conductive additives are rigid in nature and help enhance the electronic conductivity of the active layers. The polymer binder holds the active particles together and allows for homogeneous dispersion of active particles. The anode and cathode ink compositions used in this work are based on the previously reported work from our research group [62]. Using a 6 wt% of polyvinylidene fluoride (PVDF) in N-methyl-pyrrolidone (NMP), 4.5 wt% of graphite (SFG 6 L), and 1.5 wt% carbon black (Super C65), an 88 wt% LCO film dried at room temperature was obtained. In the anode, instead of the conventional PVDF binder, an aqueous-based polystyrene butadiene rubber (PSBR) binder was used. Based on recent reports, an improvement in electrochemical performance [63,64] and mechanical strength [62] was observed using PSBR as a binder in anodes. For the anode slurry, a 5.4 wt% PSBR in deionized water, 4.4 wt% of carbon black (Super C65) was used to achieve a 90.2 wt% synthetic graphite film.

2.1.3. Battery fabrication

To minimize the battery footprint, a vertical configuration is adopted where cathode and anode layers are stacked on top of one another rather than being deposited side by side. Fig. 1 (B) shows the key steps involved in the battery fabrication process. First, thin films of Cu and Al were deposited on the anode and cathode substrates, respectively, using thermal evaporation to act as the current collectors. A four-point probe setup was used to measure the sheet resistance of current collectors. The probe has four pins in contact with the current collector, two pins apply a current, and the voltage is measured across the other two pins. The sheet resistance was calculated using the current, voltage, and geometry of the sample. The sheet resistance for the evaporated Cu and Al films was recorded to be 0.27 and 0.38 ohms/sq respectively. Next, with the help of a laser ablation tool, square electrode patterns were cut into a polyimide plastic sheet to be used as stencils during the electrode slurry deposition. Stencils with various square openings were obtained to define the electrodes with areas of 25, 9, 4, and 1 mm^2. Then, the cathode and anode slurries were stencil-printed over 200 nm thick, thermally evaporated Al and Cu current collectors, respectively. The printed electrodes are shown in Fig. S1 in the Supporting Information. The miniature batteries were prepared by placing the LiPF$_6$ soaked polypropylene-based separator (20 μm, Celgard) between the LCO
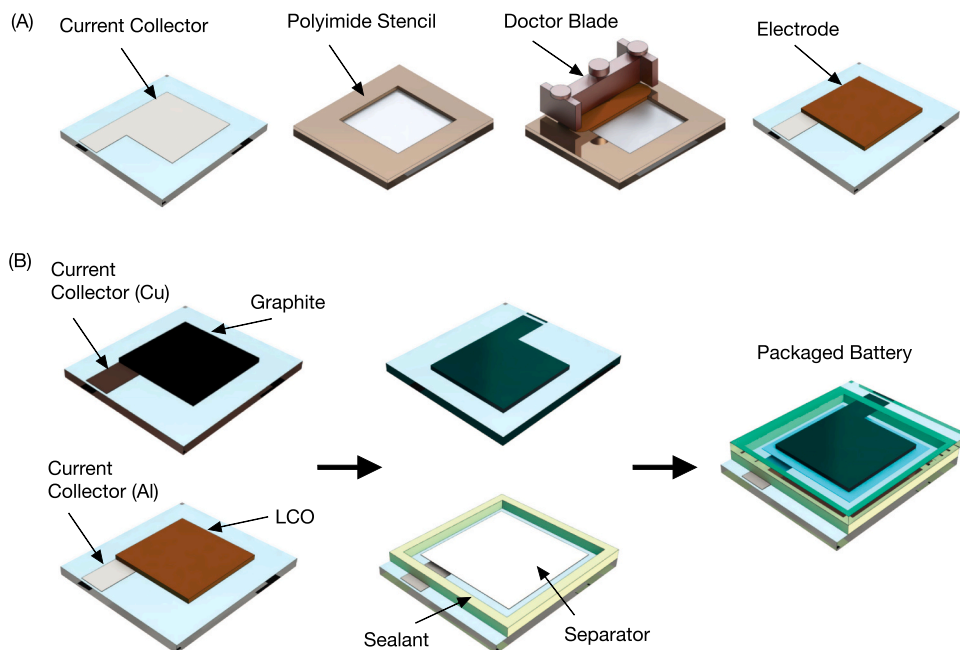
Fig. 1. (A) Stencil printing process: A plastic stencil with the square electrode pattern is placed on the substrate, and a doctor blade is moved over the stencil, which pushes the ink into the stencil, forming the printed film. (B) Schematic representation of the battery fabrication process. First, the anode (graphite) and cathode (LCO) slurries were deposited over the Cu and Al current collectors, respectively, using stencil printing. The miniature Li-ion batteries were prepared by stacking the cathode and anode with a polypropylene separator (soaked in $LiPF_6$ electrolyte) and packaging using an adhesive sealant.

cathode and graphite anode. After assembly, batteries were packaged using an airtight seal to allow testing of the batteries outside the glovebox. To package the cell stack, current collectors were sealed together with an epoxy resin (Torr Seal®) applied along the electrode edges. Fig. S1 shows a Li-ion battery with an active area of 25 mm² after packaging. Torr Seal® is a two-component epoxy and has been widely used in the vacuum industry as an excellent sealer to prevent leaks in

vacuum systems. Once the adhesive is applied, the batteries were allowed to rest for 24 h at room temperature inside the glovebox. This is to both ensure the curing of the Torr Seal® and the complete wetting of the electrodes.
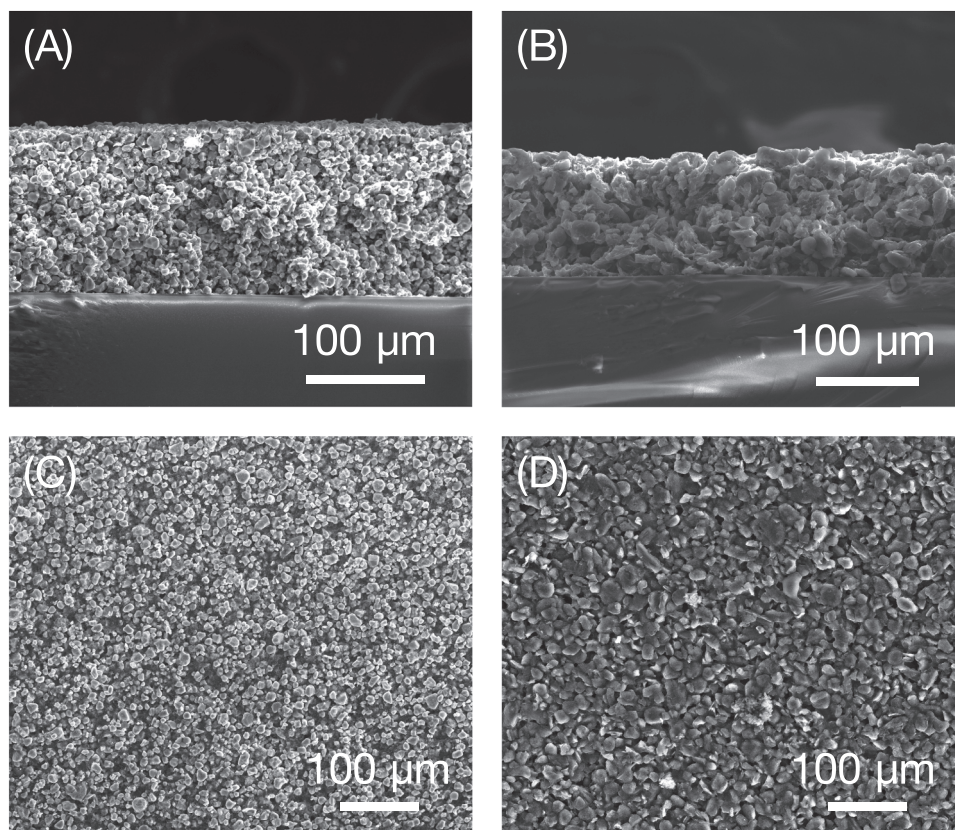
Fig. 2. Cross-sectional SEM micrographs of LCO (A) and graphite (B) electrodes. Topographical SEM micrographs of LCO (C) and graphite (D) electrodes.

2.2. Battery characterization and testing

After printing of electrode slurries, the morphology of the electrode films was characterized using scanning electron microscopy (SEM). Fig. 2 (A)-(D) show the cross-sectional and topographical SEM micrograph images of the LCO and graphite electrodes. The size of the active LCO particles ranges between 3 and 10 µm. The graphite particles have an average size of ~20 µm. According to the SEM images (Fig. 2), the active materials and conductive additives are well distributed in the electrode film. The thickness of the LCO and graphite electrodes after printing was around 100 and 80 µm, respectively.

To evaluate the electrochemical performance as a function of electrode area, battery electrodes with active areas of 25, 9, 4, and 1 mm^2 were tested. The areal loadings of the cathode for the 25, 9, 4, and 1 mm^2 electrodes were 25.8, 24.9, 23.5, and 20 mg/cm^2 respectively. For anodes, the areal loadings were measured to be 11, 12, 11.6, and 10.4 mg/cm^2 for the 25, 9, 4, and 1 mm^2 electrodes respectively. An electrolyte volume of 8, 4, 2 and 1 µL was used during the assembly and packaging of 25, 9, 4 and 1 mm^2 cells respectively. The electrolyte amount was determined based on previous studies reporting an electrolyte volume of 1.9–3 times the total pore volume as optimal for Li-ion batteries [65,66]. Before performing the desired tests, the batteries were cycled thrice at 47, 16, 10, and 10 µA for the 25, 9, 4, and 1 mm^2 electrodes respectively between 3.0 and 4.2 V. During the formation

cycle, the coulombic efficiency was in the 68–85% range; this is due to the irreversible consumption of Li ions in the formation of solid electrolyte interphase (SEI) layer and the side reactions with contaminants present in the electrode. [67–69] The columbic efficiency was around 95–99% after the completion of the formation cycle. Fig. 3 (A-D) shows the charge-discharge characteristics of the batteries with active areas in the 1–25 mm^2 range, after the completion of the battery formation cycles. The cells with 25 mm^2 active area demonstrated an average capacity of 0.84 mAh, and the average specific capacity was estimated to be 130 mAh/g, which is in good agreement with the theoretical value of 145 mAh/g for LCO. The average capacities of 280, 120, and 22 µAh were observed for batteries with active areas of 9, 4, and 1 mm^2, respectively. And, the specific capacities for the 9, 4, and 1 mm^2 was calculated to be 125, 128 and 110 mAh/g respectively. The charge-discharge curves in Fig. 3 (A-D) match the results previously obtained for Li-ion full cells with LCO cathode and graphite anode [70]. These results suggest that no apparent limitations in the electrochemical behavior of Li-ion batteries were observed as the active areas are scaled down to 1 mm^2.

Fig. 4 (A) shows a comparison of the discharged areal capacities as a function of the electrode area. For 25, 9, and 4 mm^2 electrodes, areal capacities ranged between 3 and 4 mAh/cm^2. 1 mm^2 electrode demonstrated an areal capacity of ~2.4 mAh/cm^2. This deviation in the areal capacity in case of electrodes with an active area of 1 mm^2 is
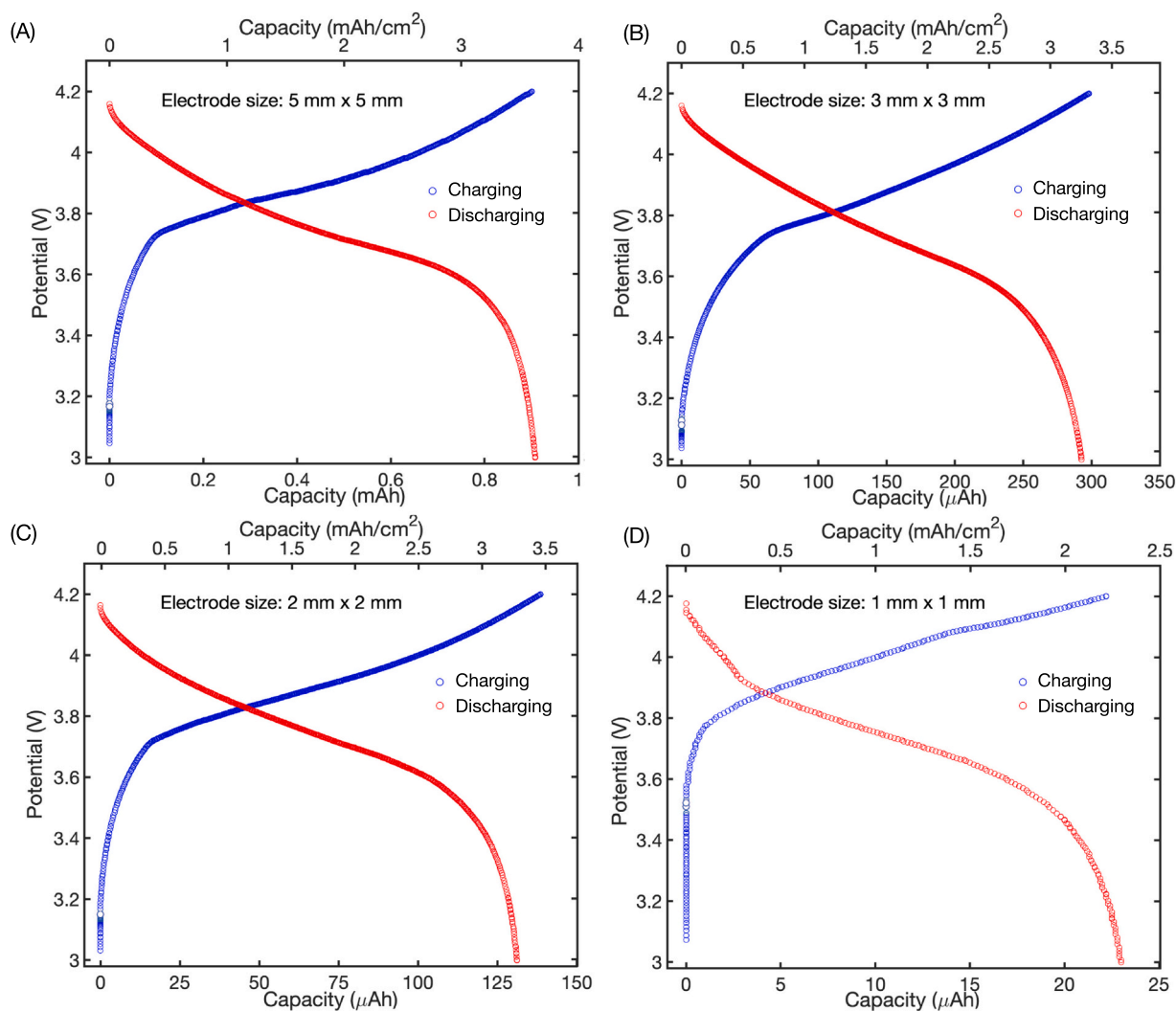

Fig. 3. Galvanostatic charge-discharge characteristics for the batteries cycled between 3.0 and 4.2 V with an active area of (A) 25 mm^2 (B) 9 mm^2 (C) 4 mm^2 and (D) 1 mm^2.
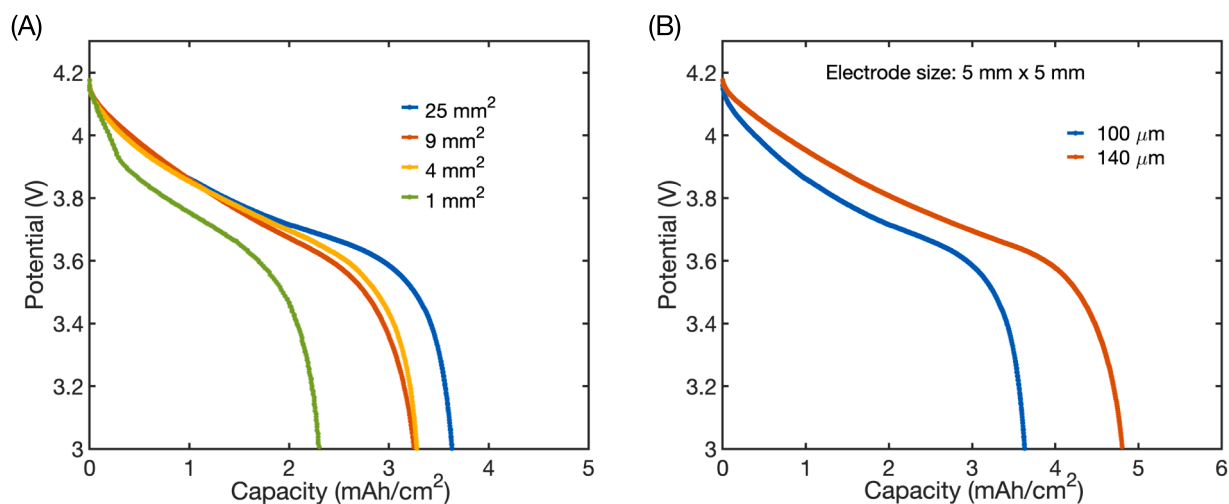
Fig. 4. (A) Discharge profiles of the Li-ion batteries with 25, 9, 4 and 1 mm^2 stencil-printed electrodes. (b) Effect of LCO cathode film thickness on the areal capacity of 25 mm^2 electrodes.

attributed to issues such as lack of complete overlap of the anode and cathode active areas; a potential result of misalignment during the battery assembly yielding reduced overall active area, and reduced compaction at the electrode edges. These capacity values can be further improved with industrial packaging processes.

To enhance the areal capacity, print parameters were modified to deposit thicker electrode films and achieve high capacity electrodes. The cathode layer thickness was increased to 140 μm. To maintain a constant ratio of the theoretical capacity of the anode to cathode (Ratio = 1.08), the doctor blade height was appropriately increased, resulting in a graphite film thickness of around 120 μm. Fig. 4 (B) shows the discharge profiles for the stencil-printed electrodes with the highest areal capacity for each cathode thickness, 100 and 140 μm. The specific capacity for the 140 μm thick LCO electrodes was 127.7 mAh/g. An areal capacity of 4.8 mAh/cm^2 was recorded for 140 μm thick LCO electrodes, ~1.3 times the areal capacity observed in the case of 100 μm thick electrodes. The enhancement in the areal capacity is attributed to the increased cathode active material loading obtained in case of 140 μm thick cathodes. Specifically, the areal loading for the 140 μm cathodes was 37.6 mg/cm^2 as compared to 25.8 mg/cm^2 for the 100 μm cathodes. Fig. S2 in the Supporting Information shows the effect of an increase in LCO cathode layer thickness on the areal capacity of 9 and 4 mm^2 electrodes. An enhancement of ~26% in the areal capacity was observed for the 9 and 4 mm^2 batteries with 140 μm thick LCO electrodes.

To evaluate the cycling performance, Li-ion batteries (active area: 25 mm^2, areal capacity of 4.8 mAh/cm^2) were cycled at the C/10 rate (136 μA based on the theoretical capacity of the cathode) between 3.0 and 4.2 V. Fig. S3 (A) in the Supporting Information shows the capacity retention and columbic efficiency of the battery. A minimum decay in the capacity occurs up to 30 cycles. The battery was able to retain 80% of its capacity up to 30 cycles, and the columbic efficiency of the battery was more than 97%. The reduction in capacity can be attributed to the quality of the packaging material i.e. adhesive sealant (Torr Seal®) surrounding the active part of these lab-scale Li-ion batteries. These capacity values can be further improved with industrial packaging processes. Next, the rate capability of the miniature Li-ion batteries (active area: 25 mm^2) was studied at rates of C/10–1 C (1.36 mA) between 4.2 V and 3.0 V. Between discharging cycles, the battery was charged using a constant current-constant voltage procedure i.e., battery was charged to 4.2 V at C/10 rate, and then it was held at a constant voltage of 4.2 V for 1 h. Fig. S3 (B) in the Supporting Information shows the discharge curves of the batteries discharged at C/10, C/5, C/2 and 1 C rates. A voltage drop at the beginning of discharge at 1 C rate was observed; this is attributed to the contact losses between the current

collector and the active layer, conductivity of the electrolyte, and the particle-particle contact resistance. With the increase in the C-rate, a drop in the areal capacity was observed beyond C/10 rate, e.g., at 1 C rate, the areal capacity was reduced to 27.2% of the capacity observed at C/10, this is comparable to the reduction in the discharge capacity reported previously for (150 μm) thick LCO electrodes [54]. Fig. S4 shows the discharge profiles at C/10, C/5, C/2, and 1 C rates for (A) 9 mm^2 batteries with a cathode film thickness of 136 μm, and (B) 25 mm^2 batteries, cathode film thickness of 98 μm.

Next, to evaluate the effectiveness of the miniaturized Li-ion batteries as a power source for IoT applications, a wireless sensor node on-chip, single-chip micro mote (SCµM), presented by Maksimovic et al. [8] was used as the load. SCµM is a wireless transceiver including a Bluetooth low-energy (BLE) transmitter and an IEEE 802.15.4 2.4 GHz transceiver integrated with a sensor interface and a Cortex M0 processor integrated on a single 3 × 2 mm^2 silicon die that requires no external components other than a power supply for operation. The test procedure was designed to determine the battery's capacity under low average but high instantaneous current loads which is more representative of duty-cycled operation often associated with IoT devices[71]. Fig. S5 in the Supporting Information shows a schematic of the test circuit used. First, the chip's transmitter was activated for 10 ms with approximately 4 mA current draw, then, after the transmitter was deactivated, the receiver was activated for 30 ms with approximately 2.8 mA current draw. Then, the chip's radio was turned off completely, as shown in Fig. 5 (A), leaving a baseline current of 700 µA. This cycle was repeated at a rate of 1 Hz and is a loose approximation of a wireless sensor node's activity in a network with a transmission of data followed by waiting for acknowledgment of reception.

For these tests, considering the typical transmitter/receiver current draw, batteries with an active area of 25 mm^2 were used. As demonstrated in Fig. 4 (B), 25 mm^2 electrodes (140 μm thick LCO) show capacity of around 1.2 mAh which is further enhanced to ~1.6 mAh on increasing the cathode film thickness to 180 μm. The areal capacity of 6.4 mAh/cm^2, volumetric capacity of 191 mAh/cm^3 and areal energy density of 23.6 mWh/cm^2 was obtained. The specific capacity was 128.8 mAh/g which is comparable to the theoretical specific capacity of LCO (145 mAh/g). Fig. S6 in the Supporting Information shows the galvanostatic charge/discharge characteristics for the 1.6 mAh battery. Fig. 5 (B) and (C) show the battery voltage and the load current as time progresses for the 1.2 and 1.6 mAh batteries under the specified duty cycle. The miniaturized batteries could support the SCµM power requirements for about 24 min before charging was required, which is reasonable considering that the peak currents ranged between 2.8 and 4 mA, and
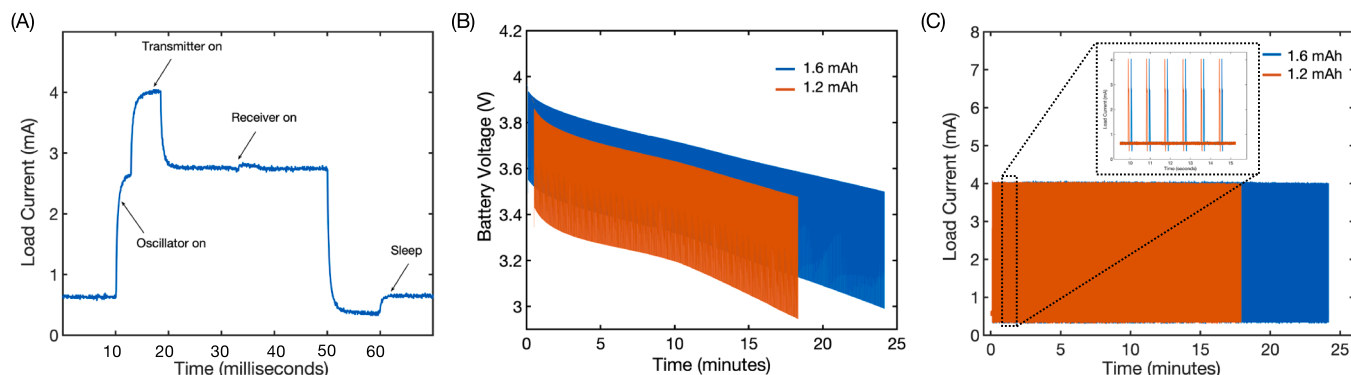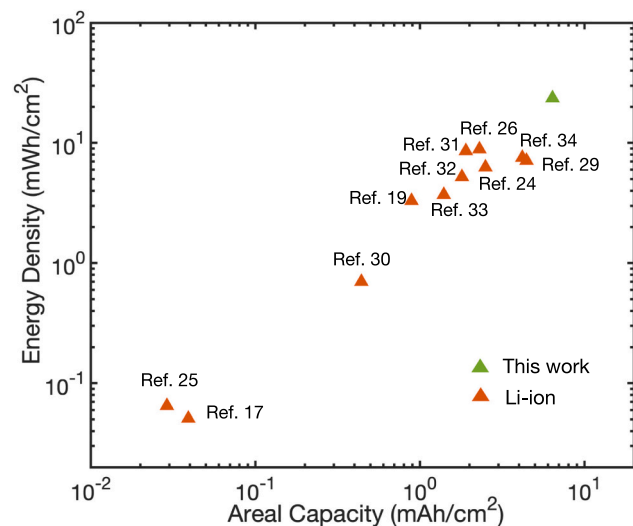
Fig. 5. (A) Load cycle used for testing: chip's transmitter activated for 10 ms with approximately 4 mA current draw, transmitter deactivated, and the receiver activated for 30 ms with approximately 2.8 mA current draw. (B) Discharge curves and (C) Current drawn by the load over the lifetime of the batteries. Batteries with capacities of 1.2 and 1.6 mAh were used. The inset in (C) shows load current waveforms over a few load cycles.

the average current drawn by the chip was around 650 µA. The large current transients do appear to degrade the lifetime. Using a switching regulator to efficiently convert the battery voltage to the desired chip supply voltage would reduce the peak and average load current by a factor of more than 2. Typical transmission and reception times in 802.15.4 networks are roughly 10 times shorter than the profile shown in Fig. 5 (A)[71]. Further, baseline current for SCµM chips has been reduced to 0.15 mA[72]. These results provide strong evidence that the printed, miniaturized Li-ion batteries are capable of supporting power requirements for next-generation IoT devices for hours to days.

Fig. 6 compares the areal capacity and energy density of our Li-ion miniature batteries with other micro-batteries reported in the literature[17,19,24–27,30–34]. Each data value plotted in Fig. 6 is tabulated in Table S1 in the Supporting Information. Compared to recent research reports on thin-film, thick-film and 3D micro-batteries, the areal capacity and energy density of our battery are considerably higher.

3. Conclusions

In summary, we have developed a fabrication process to produce miniature Li-ion batteries by combining the stencil printing process to deposit thick high capacity electrodes and an adhesive based battery sealing method, with active areas as small as 1 mm^2. Areal capacities as high as 6.4 mAh/cm^2 and areal energy density of 23.6 mWh/cm^2 were

recorded for batteries with 25 mm^2 area, 180 µm thick LCO cathode films. Further, we demonstrated that the capacity of the battery is sufficient to support the power requirements of a MEMS-based wireless sensor system. These batteries with high areal discharge capacity are ideal for applications requiring a power source with high energy density and small footprint such as in autonomous wireless sensor nodes, and miniaturized electronic systems in medical devices.

4. Experimental section

4.1. LCO and graphite inks

Cathode slurries were prepared with a 10 wt% polyvinylidene fluoride (PVDF, Kureha Corp.) in N-methyl-pyrrolidene (NMP, Sigma Aldrich) as the solvent. The binder was homogenized on the vortex mixer for 2 h. Next, 88 wt% LCO (MTI corp.), and conductive additive (4.5 wt% of graphite (SFG 6 L) and 1.5 wt% carbon black (Super C65)) was added to the binder solution, and the mixture was further homogenized on a vortex mixer for 12 h. Similarly, anode slurry was prepared by homogenizing a mixture of 4.4 wt% of carbon black (Super C65, TIMCAL), 90.2 wt% synthetic graphite (MTI Cop.), and 5.4 wt% PSBR (Targray Technology) in deionized water.

4.2. Battery processing and packaging

The slurries were stencil printed on the evaporated current collector films with a doctor blade at a speed of 10 mm/s. The blade height was adjusted to achieve the desired loading. The electrodes were dried in an oven at 80 °C for 2 h. The SEM micrographs were taken using a tabletop SEM (FEI Quanta 3D). Before assembling the battery in the glove box, the electrodes were heated overnight in a vacuum oven connected to the glove box at 140 °C for 12 h to remove traces of residual solvent from the electrodes.

4.3. Electrochemical characterization

All measurements are carried out in the air and at room temperature. A battery analyzer, BST-8A (MTI Corp), was used to characterize the electrochemical performance of the battery. During the formation cycles, the batteries were cycled between 4.2 V and 3.0 V for three cycles. For subsequent electrochemical experiments, the C-rate was estimated based on the discharged capacity at the end of the formation cycle. For the rate test, the charge rate was maintained at C/10, and discharge rates were varied from C/10–1 C. The cycling life is also measured in constant current, and both the charge and discharge rates are fixed at C/10.

Fig. 6. Comparison of areal energy density (mWh/cm^2) and areal capacity (mAh/cm^2) of our battery with other micro-batteries based on Li-ion chemistry reported in the literature.

4.4. Battery powering wireless sensor node

A single-chip micro mote (SCµM)[8] was used as the load, the device has an IEEE 802.15.4 compatible transmitter and receiver, and a Cortex M0 running with a 5 MHz clock frequency. The Cortex was running at 5 MHz for the duration of the experiment. The code running on the processor was a loose approximation of wireless communication with transmitter and receiver activated, one after the other, with a delay, in a constantly repeating loop that would only cease when the device was disconnected. Because the device has no non-volatile memory, it was programmed, which added some small additional charge draw from the battery. To measure the current, a 20 Ω sense resistor was placed in series with the battery, and a National Instruments DAQ was used to perform a 16-bit 20 kS/s voltage measurement across it. The battery voltage was also observed with a Fluke multimeter with approximately 2 MΩ resistance. When the observed voltage dropped below 20% of the battery's open-circuit voltage, the system was manually disconnected. Since the SCµM chip was manufactured with standard TSMC 65 nm devices, a battery with potential > 3.3 V would destroy the chip. Therefore, an ADP1713 linear series regulator was used with a 10 µF load capacitor (necessary for circuit stability) to regulate the local supply to 1.5 V. The current shown in Fig. 6 (C) includes both the power drawn by the chip and by the low-dropout regulator.

CRediT authorship contribution statement

Anju Toor: Conceptualization, Methodology, Investigation, Validation, Writing, Visualization, Supervision. **Albert Wen**: Validation. **Filip Maksimovic**: Investigation, Writing. **Abhinav M. Gaikwad**: Writing. **Kristofer S.J. Pister**: Writing, Supervision, Funding acquisition. **Ana C. Arias**: Methodology, Writing, Supervision, Funding acquisition.

Declaration of Competing Interest

The authors declare that they have no known competing financial interests or personal relationships that could have appeared to influence the work reported in this paper.

Acknowledgements

Appendix A. Supporting information

Supplementary data associated with this article can be found in the online version at doi:10.1016/j.nanoen.2020.105666.

References

[1] I. Suciu, F. Maksimovic, B. Wheeler, D.C. Burnett, O. Khan, T. Watteyne, X. Vilajosana, K.S.J. Pister, Dynamic channel calibration on a crystal-free mote-on-a-chip, IEEE Access 7 (2019) 120884–120900, https://doi.org/10.1109/access.2019.2937689.

[2] C. Zhang, J. Xu, W. Ma, W. Zheng, PCR microfluidic devices for DNA amplification, Biotechnol. Adv. 24 (2006) 243–284, https://doi.org/10.1016/j.biotechadv.2005.10.002.

[3] D.C. Burnett, H.M. Fahad, L. Lee, F. Maksimovic, B. Wheeler, O. Khan, A. Javey, K. S. J. Pister, Proceedings of the 2019 20th International Conference Solid-State Sensors, Actuators Microsystems Eurosensors XXXIII, TRANSDUCERS 2019 EUROSENSORS XXXIII, 2019.

[4] Y. Shao, S. Shao, M. Xu, S. Song, Z. Tian, An inertial piezoelectric actuator with miniaturized structure and improved load capacity, Smart Mater. Struct. 28 (2019), 055023, https://doi.org/10.1088/1361-665X/ab0eb9.

[5] P.S. Waggoner, H.G. Craighead, Micro- and nanomechanical sensors for environmental, chemical, and biological detection, Lab Chip 7 (2007) 1238, https://doi.org/10.1039/b707401h.

[6] H. Yao, A.J. Shum, M. Cowan, I. Lähdesmäki, B.A. Parviz, A contact lens with embedded sensor for monitoring tear glucose level, Biosens. Bioelectron. 26 (2011) 3290–3296, https://doi.org/10.1016/j.bios.2010.12.042.

[7] B.L. Smarr, D.C. Burnett, S.M. Mesri, K.S.J. Pister, L.J. Kriegsfeld, A wearable sensor system with circadian rhythm stability estimation for prototyping biomedical studies, IEEE Trans. Affect. Comput. 7 (2016) 220–230, https://doi.org/10.1109/TAFFC.2015.2511762.

[8] F. Maksimovic, B. Wheeler, D.C. Burnett, O. Khan, S. Mesri, I. Suciu, L. Lee, A. Moreno, A. Sundararajan, B. Zhou, R. Zoll, A. Ng, T. Chang, X. Villajosana, T. Watteyne, A. Niknejad, K.S.J. Pister, IEEE Symp. VLSI Circuits Dig. Tech. Pap. 2019.

[9] J. Deng, X. Lu, L. Liu, L. Zhang, O.G. Schmidt, Introducing rolled-up nanotechnology for advanced energy storage devices, Adv. Energy Mater. 6 (2016), 1600797, https://doi.org/10.1002/aenm.201600797.

[10] X. Li, M. Gu, S. Hu, R. Kennard, P. Yan, X. Chen, C. Wang, M.J. Sailor, J.G. Zhang, J. Liu, Mesoporous silicon sponge as an anti-pulverization structure for high-performance lithium-ion battery anodes, Nat. Commun. 5 (2014) 4105, https://doi.org/10.1038/ncomms5105.

[11] X. Chen, H. Zhu, Y.C. Chen, Y. Shang, A. Cao, L. Hu, G.W. Rubloff, MWCNT/V2O5core/shell sponge for high areal capacity and power density Li-Ion cathodes, ACS Nano 6 (2012) 7948–7955, https://doi.org/10.1021/nn302417x.

[12] L. Liu, H. Guo, J. Liu, F. Qian, C. Zhang, T. Li, W. Chen, X. Yang, Y. Guo, Self-assembled hierarchical yolk–shell structured NiO@C from metal–organic frameworks with outstanding performance for lithium storage, Chem. Commun. 50 (2014) 9485–9488, https://doi.org/10.1039/c4cc03807j.

[13] M.R. Lukatskaya, B. Dunn, Y. Gogotsi, Multidimensional materials and device architectures for future hybrid energy storage, Nat. Commun. 7 (2016) 12647, https://doi.org/10.1038/ncomms12647.

[14] Y. Wang, B. Liu, Q. Li, S. Cartmell, S. Ferrara, Z.D. Deng, J. Xiao, Lithium and lithium ion batteries for applications in microelectronic devices: a review, J. Power Sources 286 (2015) 330–345, https://doi.org/10.1016/j.jpowsour.2015.03.164.

[15] M. Koo, K. Il Park, S.H. Lee, M. Suh, D.Y. Jeon, J.W. Choi, K. Kang, K.J. Lee, Bendable inorganic thin-film battery for fully flexible electronic systems, Nano Lett. 12 (2012) 4810–4816, https://doi.org/10.1021/nl302254v.

[16] W. Liu, M.S. Song, B. Kong, Y. Cui, Flexible and stretchable energy storage: recent advances and future perspectives, Adv. Mater. 29 (2017), 1603436, https://doi.org/10.1002/adma.201603436.

[17] F. Le Cras, B. Pecquenard, V. Dubois, V.P. Phan, D. Guy-Bouyssou, All-solid-state lithium-ion microbatteries using silicon nanofilm anodes: high performance and memory effect, Adv. Energy Mater. 5 (2015), 1501061, https://doi.org/10.1002/aenm.201501061.

[18] H.S. Lee, S. Kim, K.B. Kim, J.W. Choi, Scalable fabrication of flexible thin-film batteries for smart lens applications, Nano Energy 53 (2018) 225–231, https://doi.org/10.1016/j.nanoen.2018.08.054.

[19] S. Oukassi, R. Salot, A. Bazin, C. Secouard, I. Chevalier, S. Poncet, S. Poulet, J. M. Boissel, F. Geffraye, J. Brun, International Electron Devices Meeting. IEDM Technical Digest, Institute Of Electrical And Electronics Engineers Inc.,, 2019.

[20] R. Kumar, K.M. Johnson, N.X. Williams, V. Subramanian, Scaling printable Zn–Ag2O batteries for integrated electronics, Adv. Energy Mater. 9 (2019), 1803645, https://doi.org/10.1002/aenm.201803645.

[21] H. Kim, J. Proell, R. Kohler, W. Pfleging, A. Pique, Laser-printed and processed LiCoO2 cathodethick films for li-ion microbatteries, J. Laser Micro/Nanoeng. 7 (2012) 320–325, https://doi.org/10.2961/jlmn.2012.03.0016.

[22] J. Pröll, H. Kim, A. Piqué, H.J. Seifert, W. Pfleging, Laser-printing and femtosecond-laser structuring of LiMn2O4 composite cathodes for Li-ion microbatteries, J. Power Sources 255 (2014) 116–124, https://doi.org/10.1016/j.jpowsour.2013.12.132.

[23] W. Lai, C.K. Erdonmez, T.F. Marinis, C.K. Bjune, N.J. Dudney, F. Xu, R. Wartena, Y. M. Chiang, Ultrahigh-energy-density microbatteries enabled by new electrode architecture and micropackaging design, Adv. Mater. 22 (2010) E139–E144, https://doi.org/10.1002/adma.200903650.

[24] M. Nasreldin, R. Delattre, C. Calmes, M. Ramuz, V.A. Sugiawati, S. Maria, J.L. de, B. de la Tocnaye, T. Djenizian, High performance stretchable Li-ion microbattery, Energy Storage Mater. 33 (2020) 108–115.

[25] H. Ning, J.H. Pikul, R. Zhang, X. Li, S. Xu, J. Wang, J.A. Rogers, W.P. King, P. V. Braun, Holographic patterning of high-performance on-chip 3D lithium-ion microbatteries, Proc. Natl. Acad. Sci. U.S.A. 112 (2015) 6573–6578, https://doi.org/10.1073/pnas.1423889112.

[26] L. Zhou, W. Ning, C. Wu, D. Zhang, W. Wei, J. Ma, C. Li, L. Chen, 3D-printed microelectrodes with a developed conductive network and hierarchical pores toward high areal capacity for microbatteries, Adv. Mater. Technol. (2018), 1800402, https://doi.org/10.1002/admt.201800402.

[27] L. Airoldi, U. Anselmi-Tamburini, B. Vigani, S. Rossi, P. Mustarelli, E. Quartarone, Additive manufacturing of aqueous-processed LiMn2O4Thick electrodes for high-energy-density lithium-ion batteries, Batter. Supercaps 3 (2020) 1040–1050, https://doi.org/10.1002/batt.202000058.

[28] W. Si, I. Mönch, C. Yan, J. Deng, S. Li, G. Lin, L. Han, Y. Mei, O.G. Schmidt, A single rolled-up Si tube battery for the study of electrochemical kinetics, electrical conductivity, and structural integrity, Adv. Mater. 26 (2014) 7973–7978, https://doi.org/10.1002/adma.201402484.

[29] K. Sun, T.S. Wei, B.Y. Ahn, J.Y. Seo, S.J. Dillon, J.A. Lewis, 3D printing of interdigitated li-ion microbattery architectures, Adv. Mater. 25 (2013) 4539–4543, https://doi.org/10.1002/adma.201301036.

[30] T.S. Wei, B.Y. Ahn, J. Grotto, J.A. Lewis, 3D printing of customized li-ion batteries with thick electrodes, Adv. Mater. 30 (2018), 1703027, https://doi.org/10.1002/adma.201703027.

[31] M. Cheng, Y. Jiang, W. Yao, Y. Yuan, R. Deivanayagam, T. Foroozan, Z. Huang, B. Song, R. Rojaee, T. Shokuhfar, Y. Pan, J. Lu, R. Shahbazian-Yassar, Elevated-temperature 3D printing of hybrid solid-state electrolyte for li-ion batteries, Adv. Mater. 30 (2018), 1800615, https://doi.org/10.1002/adma.201800615.

[32] K. Fu, Y. Wang, C. Yan, Y. Yao, Y. Chen, J. Dai, S. Lacey, Y. Wang, J. Wan, T. Li, Z. Wang, Y. Xu, L. Hu, Graphene oxide-based electrode inks for 3D-printed lithium-ion batteries, Adv. Mater. 28 (2016) 2587–2594, https://doi.org/10.1002/adma.201505391.

[33] J.I. Hur, L.C. Smith, B. Dunn, High areal energy density 3D lithium-ion microbatteries, Joule 2 (2018) 1187–1201, https://doi.org/10.1016/j.joule.2018.04.002.

[34] D.S. Ashby, C.S. Choi, M.A. Edwards, A.A. Talin, H.S. White, B.S. Dunn, High-performance solid-state lithium-ion battery with mixed 2D and 3D electrodes, ACS Appl. Energy Mater. 3 (2020) 8402–8409, https://doi.org/10.1021/acsaem.0c01029.

[35] J.B. Bates, N.J. Dudney, B. Neudecker, A. Ueda, C.D. Evans, Thin-film lithium and lithium-ion batteries, Solid State Ion. 135 (2000) 33–45, https://doi.org/10.1016/S0167-2738(00)00327-1.

[36] N.J. Dudney, Y. Il Jang, Analysis of thin-film lithium batteries with cathodes of 50 nm to 4 μm thick LiCoO2, J. Power Sources 119–121 (2003) 300–304.

[37] B.J. Neudecker, N.J. Dudney, J.B. Bates, Lithium-free" thin-film battery with in situ plated Li anode, J. Electrochem. Soc. 147 (2000) 517, https://doi.org/10.1149/1.1393226.

[38] C.L. Liao, K.Z. Fung, Lithium cobalt oxide cathode film prepared by rf sputtering, J. Power Sources 128 (2004) 263–269, https://doi.org/10.1016/j.jpowsour.2003.09.065.

[39] W.G. Choi, S.G. Yoon, Structural and electrical properties of LiCoO2 thin-film cathodes deposited on planar and trench structures by liquid-delivery metalorganic chemical vapour deposition, J. Power Sources 125 (2004) 236–241, https://doi.org/10.1016/j.jpowsour.2003.08.014.

[40] Y. Iriyama, M. Inaba, T. Abe, Z. Ogumi, Preparation of c-axis oriented thin films of LiCoO2 by pulsed laser deposition and their electrochemical properties, J. Power Sources 94 (2001) 175–182, https://doi.org/10.1016/S0378-7753(00)00580-2.

[41] S.J. Dillon, K. Sun, Microstructural design considerations for Li-ion battery systems, Curr. Opin. Solid State Mater. Sci. 16 (2012) 153–162, https://doi.org/10.1016/j.cossms.2012.03.002.

[42] S. Ferrari, M. Loveridge, S.D. Beattie, M. Jahn, R.J. Dashwood, R. Bhagat, Latest advances in the manufacturing of 3D rechargeable lithium microbatteries, J. Power Sources 286 (2015) 25–46, https://doi.org/10.1016/j.jpowsour.2015.03.133.

[43] D.R. Rolison, J.W. Long, J.C. Lytle, A.E. Fischer, C.P. Rhodes, T.M. McEvoy, M. E. Bourg, A.M. Lubers, Multifunctional 3D nanoarchitectures for energy storage and conversion, Chem. Soc. Rev. 38 (2009) 226–252, https://doi.org/10.1039/b801151f.

[44] J.W. Long, B. Dunn, D.R. Rolison, H.S. White, Three-dimensional battery architectures, Chem. Rev. 104 (2004) 4463–4492, https://doi.org/10.1021/cr020740l.

[45] A.M. Gaikwad, D.A. Steingart, T. Nga Ng, D.E. Schwartz, G.L. Whiting, A flexible high potential printed battery for powering printed electronics, Appl. Phys. Lett. 102 (2013), 233302.

[46] P.H.L. Notten, F. Roozeboom, R.A.H. Niessen, L. Baggetto, 3-D integrated all-solid-state rechargeable batteries, Adv. Mater. 19 (2007) 4564–4567, https://doi.org/10.1002/adma.200702398.

[47] M. Létiche, E. Eustache, J. Freixas, A. Demortière, V. De Andrade, L. Morgenroth, P. Tilmant, F. Vaurette, D. Troadec, P. Roussel, T. Brousse, C. Lethien, Atomic layer deposition of functional layers for on chip 3D li-ion all solid state microbattery, Adv. Energy Mater. 7 (2017), 1601402, https://doi.org/10.1002/aenm.201601402.

[48] J. Ren, L. Li, C. Chen, X. Chen, Z. Cai, L. Qiu, Y. Wang, X. Zhu, H. Peng, Twisting carbon nanotube fibers for both wire-shaped micro-supercapacitor and micro-battery, Adv. Mater. 25 (2013) 1155–1159, https://doi.org/10.1002/adma.201203445.

[49] D. Ruzmetov, V.P. Oleshko, P.M. Haney, H.J. Lezec, K. Karki, K.H. Baloch, A. K. Agrawal, A.V. Davydov, S. Krylyuk, Y. Liu, J. Huang, M. Tanase, J. Cumings, A. A. Talin, Electrolyte stability determines scaling limits for solid-state 3D Li ion batteries, Nano Lett. 12 (2012) 505–511, https://doi.org/10.1021/nl204047z.

[50] J.H. Pikul, H. Gang Zhang, J. Cho, P.V. Braun, W.P. King, High-power lithium ion microbatteries from interdigitated three-dimensional bicontinuous nanoporous electrodes, Nat. Commun. 4 (2013) 1732, https://doi.org/10.1038/ncomms2747.

[51] C.P. Rhodes, J.W. Long, K.A. Pettigrew, R.M. Stroud, D.R. Rolison, Architectural integration of the components necessary for electrical energy storage on the nanoscale and in 3D, Nanoscale 3 (2011) 1731, https://doi.org/10.1039/c0nr00731e.

[52] C.C. Ho, J.W. Evans, P.K. Wright, Direct write dispenser printing of a zinc microbattery with an ionic liquid gel electrolyte, J. Micromech. Microeng. 20 (2010), 104009, https://doi.org/10.1088/0960-1317/20/10/104009.

[53] C.C. Ho, K. Murata, D.A. Steingart, J.W. Evans, P.K. Wright, A super ink jet printed zinc–silver 3D microbattery, J. Micromech. Microeng. 19 (2009), 094013, https://doi.org/10.1088/0960-1317/19/9/094013.

[54] A.M. Gaikwad, B.V. Khau, G. Davies, B. Hertzberg, D.A. Steingart, A.C. Arias, A high areal capacity flexible lithium-ion battery with a strain-compliant design, Adv. Energy Mater. 5 (2015), 1401389, https://doi.org/10.1002/aenm.201401389.

[55] A.M. Gaikwad, A.C. Arias, D.A. Steingart, Recent progress on printed flexible batteries: mechanical challenges, printing technologies, and future prospects, Energy Technol. 3 (2015) 305–328, https://doi.org/10.1002/ente.201402182.

[56] R.E. Sousa, C.M. Costa, S. Lanceros-Méndez, Advances and future challenges in printed batteries, ChemSusChem 8 (2015) 3539–3555, https://doi.org/10.1002/cssc.201500657.

[57] K.H. Choi, D.B. Ahn, S.Y. Lee, Current status and challenges in printed batteries: toward form factor-free, monolithic integrated power sources, ACS Energy Lett. 3 (2018) 220–236, https://doi.org/10.1021/acsenergylett.7b01086.

[58] A.E. Ostfeld, A.M. Gaikwad, Y. Khan, A.C. Arias, High-performance flexible energy storage and harvesting system for wearable electronics, Sci. Rep. 6 (2016) 26122.

[59] X. Wang, X. Lu, B. Liu, D. Chen, Y. Tong, G. Shen, Flexible energy-storage devices: design consideration and recent progress, Adv. Mater. 26 (2014) 4763–4782.

[60] S.H. Kim, K.H. Choi, S.J. Cho, J. Yoo, S.S. Lee, S.Y. Lee, Flexible/shape-versatile, bipolar all-solid-state lithium-ion batteries prepared by multistage printing, Energy Environ. Sci. 11 (2018) 321–330.

[61] Y. Chen, R. Jamshidi, K. White, S. Çınar, E. Gallegos, N. Hashemi, R. Montazami, Physical-chemical hybrid transiency: A fully transient li-ion battery based on insoluble active materials, J. Polym. Sci. Part B Polym. Phys. 54 (2016) 2021–2027, https://doi.org/10.1002/polb.24113.

[62] A.M. Gaikwad, A.C. Arias, Understanding the effects of electrode formulation on the mechanical strength of composite electrodes for flexible batteries, ACS Appl. Mater. Interfaces 9 (2017) 6390–6400, https://doi.org/10.1021/acsami.6b14719.

[63] J.H. Lee, S. Lee, U. Paik, Y.M. Choi, Aqueous processing of natural graphite particulates for lithium-ion battery anodes and their electrochemical performance, J. Power Sources 147 (2005) 249–255, https://doi.org/10.1016/j.jpowsour.2005.01.022.

[64] L. Wang, Y. Fu, V.S. Battaglia, G. Liu, SBR–PVDF based binder for the application of SLMP in graphite anodes, RSC Adv. 3 (2013) 15022, https://doi.org/10.1039/c3ra42773k.

[65] S.J. An, J. Li, D. Mohanty, C. Daniel, B.J. Polzin, J.R. Croy, S.E. Trask, D.L. Wood, Correlation of electrolyte volume and electrochemical performance in lithium-ion pouch cells with graphite anodes and NMC532 cathodes, J. Electrochem. Soc. 164 (2017) A1195–A1202, https://doi.org/10.1149/2.1131706jes.

[66] B.R. Long, S.G. Rinaldo, K.G. Gallagher, D.W. Dees, S.E. Trask, B.J. Polzin, A.N. Jansen, D.P. Abraham, I. Bloom, J. Bareño, J.R. Croy, Proceedings of the 35th International Battery Seminiar and Exhibition 2018, 2018.

[67] J. Vetter, P. Novák, M.R. Wagner, C. Veit, K.C. Möller, J.O. Besenhard, M. Winter, M. Wohlfahrt-Mehrens, C. Vogler, A. Hammouche, Ageing mechanisms in lithium-ion batteries, J. Power Sources 147 (2005) 269–281, https://doi.org/10.1016/j.jpowsour.2005.01.006.

[68] D. Aurbach, M.D. Levi, E. Levi, H. Teller, B. Markovsky, G. Salitra, U. Heider, L. Heider, Common electroanalytical behavior of Li intercalation processes into graphite and transition metal oxides, J. Electrochem. Soc. 145 (1998) 3024–3034, https://doi.org/10.1149/1.1838758.

[69] D. Aurbach, Y. Talyosef, B. Markovsky, E. Markevich, E. Zinigrad, L. Asraf, J. S. Gnanaraj, H.J. Kim, Design of electrolyte solutions for Li and Li-ion batteries: a review, Electrochim. Acta 50 (2004) 247–254.

[70] A.E. Ostfeld, A.C. Arias, Flexible photovoltaic power systems: integration opportunities, challenges and advances, Flex. Print. Electron. 2 (2017), 013001.

[71] X. Vilajosana, Q. Wang, F. Chraim, T. Watteyne, T. Chang, K.S.J. Pister, A realistic energy consumption model for TSCH networks, IEEE Sens. J. 14 (2014) 482–489, https://doi.org/10.1109/JSEN.2013.2285411.

[72] A. Moreno, F. Maksimovic, L. Lee, B. Kilberg, J.S. Rentmeister, J. Stauth, C. Schindler, H. Gomez, D. Teal, D. Acker-James, A. Fearing, K. Pister, GOMACTech San. Diego 2020.